Impacts of the U(1)$_A$ anomaly on nuclear and neutron star equation of state based on a parity doublet model

Bikai Gao,[1,*] Takuya Minamikawa,[1,†] Toru Kojo,[2,3,‡] and Masayasu Harada[1,4,5,§]

[1]*Department of Physics, Nagoya University, Nagoya 464-8602, Japan*
[2]*Department of Physics, Tohoku University, Sendai 980-8578, Japan*
[3]*Key Laboratory of Quark and Lepton Physics (MOE) and Institute of Particle Physics, Central China Normal University, Wuhan 430079, China*
[4]*Advanced Science Research Center, Japan Atomic Energy Agency, Tokai 319-1195, Japan*
[5]*Kobayashi-Maskawa Institute for the Origin of Particles and the Universe, Nagoya University, Nagoya 464-8602, Japan*

(Received 14 July 2022; accepted 14 November 2022; published 26 December 2022)

We examine the role of the U(1)$_A$ anomaly in a parity doublet model of nucleons which include the chiral variant and invariant masses. Our model expresses the U(1)$_A$ anomaly by the Kobayashi-Maskawa-'t Hooft (KMT) interaction in the mesonic sector. After examining the roles of the KMT term in vacuum, we discuss its impacts on nuclear equations of state (EOS). The U(1)$_A$ anomaly increases the masses of the η' and σ mesons and enhances the chiral symmetry breaking. Also, the U(1)$_A$ anomaly enlarges the energy difference between chiral symmetric and symmetry broken vacuum; in turn, the chiral restoration at high density adds a larger energy density (often referred as a bag constant) to EOSs than in the case without the anomaly, leading to softer EOSs. Including these U(1)$_A$ effects, we update the previously constructed unified equations of state that interpolate the nucleonic EOS at $n_B \leqslant 2n_0$ ($n_0 = 0.16$ fm^{-3}; nuclear saturation density) and quark EOS at $n_B \geqslant 5n_0$. The unified EOS is confronted with the observational constraints on the masses and radii of neutron stars. The softening of EOSs associated with the $U(1)$ anomaly reduces the overall radii, relaxing the previous constraint on the chiral invariant mass m_0. Including the attractive nonlinear ρ-ω coupling for the reduced slope parameter in the symmetry energy, our new estimate is 400 MeV $\leqslant m_0 \leqslant$ 700 MeV, with m_0 smaller than our previous estimate by $\approx$200 MeV.

DOI: 10.1103/PhysRevC.106.065205

I. INTRODUCTION

The chiral SU(N_f)$_L$ $\otimes$ SU(N_f)$_R$ symmetry in quantum chromodynamics (QCD) and its spontaneous symmetry breaking (SSB) plays the key role in describing the low-energy hadron physics, e.g., the soft pion dynamics and the dynamically generated quark masses [1]. The chiral condensates, as the order parameters of the chiral SSB, quantify the degree of the chiral SSB and also are useful in characterizing states of matter in QCD at finite temperature and/or density [2,3].

In addition to the dynamical SSB, the current quark mass and the quantum anomaly explicitly break the U(1)$_A$ symmetry and assist the formation of the chiral condensates [4,5]. In this paper we study the impact of the U(1)$_A$ anomaly on the chiral symmetry breaking and examine how it influences nuclear matter equations of state (EOS). While there are many. works on nucleonic EOS emphasizing the importance of in-medium interactions among nucleons, in-medium changes of the Dirac sea structure and their impacts on EOS acquire much less attention. We argue that the U(1)$_A$ anomaly increases the discrepancy between the chiral symmetry broken and restored phases. In other words, the anomaly increases the *bag constant* associated with the chiral restoration as shown in Fig. 1. In the context of EOS, a larger bag constant adds the energy density but reduces the pressure, leading to softer EOS.

In the nuclear matter domain, we include the anomaly effects in terms of the Kobayashi-Maskawa-'t Hooft (KMT) interactions [6] for a three-flavor mesonic Lagrangian made of scalar and vector mesons. The KMT interactions relate up-, down-, and strange-quark Dirac sea even before the strangeness appears in a matter. In fact, the chiral restoration for the up- and down-quark sectors assists the chiral restoration for the strange quark sector, possibly changing the masses of hyperons in nuclear matter. Such structural changes in hyperons are potentially important for matter composition in neutron stars (NSs).

The baryonic part in this work is treated in a parity doublet model (PDM) [7,8] for nucleons in which the ordinary nucleon $N(940)$ and its parity partner $N(1535)$ form a doublet. The novel feature of the PDM is that the nucleon masses include not only the conventional chiral variant mass but also invariant mass (m_0) whose existence is supported by the previous lattice QCD simulations [9]. Accordingly, nucleons

*gaobikai@hken.phys.nagoya-u.ac.jp
†minamikawa@hken.phys.nagoya-u.ac.jp
‡torujj@nucl.phys.tohoku.ac.jp
§harada@hken.phys.nagoya-u.ac.jp

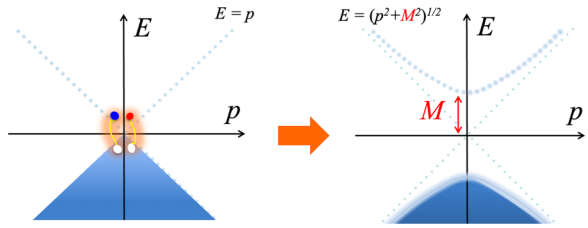

FIG. 1. The Dirac sea in chiral symmetric (left) and symmetry broken (right) phases. The particle-antiparticle pairs condense to break the chiral symmetry and produce the mass gap M. The mass gap is larger in the presence of the $U(1)_A$ anomaly. The energy difference in the Dirac sea between the chiral symmetry restored and broken phases defines (a part of) the bag constant.

in the PDM is less sensitive to the chiral condensate or σ fields than in conventional linear σ models. The PDM for vacuum physics has been studied in Refs. [7,8,10–17], and its EOS in Refs. [18–37]. The parameters of the PDM, coupled to the two-flavor mesonic sector without the $U(1)_A$ anomaly, have been tuned to fit the vacuum and the nuclear saturation properties at n_0 ($n_0 \simeq 0.16$ fm^{-3}; nuclear saturation density). In this work we retune the parameters including the $U(1)_A$ anomaly.

The key feature of the PDM, in the context of EOS, is that a greater m_0 leads to weaker σ couplings to nucleons, because a nucleon does not have to acquire its mass entirely from the σ fields. The couplings to ω fields are also smaller because, at n_0, its repulsive contributions must be balanced with the attractive σ contributions. At densities larger than n_0, however, the σ fields reduce but the ω fields increase, and these contributions no longer balance; the repulsive nature of the ω is directly reflected in the stiffness of EOS. As a consequence, a larger m_0 weakens the ω fields and softens EOS at supranuclear densities.

For applications to NS phenomenology, nuclear EOS in the PDM is extrapolated to densities beyond n_0. It has been simply extrapolated [35] or combined with a quark model assuming the quark-hadron crossover [2,11,33,36,38–40]. In the latter, the PDM EOS is used up to $2n_0$ and interpolated with the quark EOS at $\gtrsim 5n_0$ via polynomial interpolants. Including the charge neutrality and β-equilibrium conditions, the unified EOS was confronted with NS constraints from the existence of two-solar mass ($2M_\odot$) NSs [41] and the gravitational waves from the NS merger event GW170817 [42–44]. Based on the upper bound for the NS radii constraint, we previously constrained m_0 to rather large values [36], 600 MeV $\lesssim m_0 \lesssim$ 900 MeV.

In this work, we update the constraints by including the $U(1)_A$ anomaly and also include the previously neglected $\rho^2\omega^2$ terms which are usually assumed to be attractive to make EOS softer. Both effects soften EOS at low densities $\simeq$1–2n_0, leading to smaller NS radii. As a result, we obtain more relaxed constraints on m_0, 400 MeV $\lesssim m_0 \lesssim$ 700 MeV, reducing the previous range by $\sim$200–300 MeV. We also add the radius constraint from the Pulsating Source of Radiation (PSR) J0740+6620 for $2.08 \pm 0.07 M_\odot$ NS, $R_{2.08} = 12.35 \pm 0.75$ km [45], and $12.39^{+1.30}_{-0.98}$ km [46].

This paper is organized as follows. In Sec. II, we explain the formulation of our model which based on parity doublet structure. In Sec. III, we construct EOS in hadronic matter and quark matter separately and the parameters are determined in Sec. IV. Main results of the analysis are shown in Sec. VI and Sec. VII. In Sec. VIII, we show a summary and discussions.

II. FORMULATION

In this section, we construct a model of symmetric nuclear matter.

A. Scalar and pseudoscalar mesons

We first construct an effective Lagrangian for scalar and pseudoscalar mesons based on the $SU(3)_L \times SU(3)_R$ chiral symmetry [14–17] including the effect of $U(1)_A$ anomaly. Quarks transform under $SU(3)_L \times SU(3)_R \times U(1)_A$ symmetry as

$$q_L \to e^{-i\theta_A} g_L q_L, \qquad q_R \to e^{+i\theta_A} g_R q_R, \tag{1}$$

with $g_{L,R} \in SU(3)_{L,R}$ and θ_A being the transformation parameters. Accordingly, we assign the $U(1)_A$ charge of the left and right-handed quarks as -1 and $+1$, respectively. The chiral representation of the left-handed quark is then given by

$$q_L : (\mathbf{3}, \mathbf{1})_{-1}, \tag{2}$$

where these **3** and **1** in the bracket express the triplet and singlet for $SU(3)_L$ symmetry and $SU(3)_R$ symmetry, respectively. The index indicates the axial charge of the fields. On the other hand, the chiral representation of the right-handed quark is given by

$$q_R : (\mathbf{1}, \mathbf{3})_{+1}. \tag{3}$$

We introduce a 3×3 matrix field Φ for scalar and pseudoscalar mesons as

$$\Phi_{ij} : (\mathbf{3}, \bar{\mathbf{3}})_{-2}. \tag{4}$$

We adopt the meson part of the Lagrangian as

$$\mathcal{L}_M^{\rm scalar} = \mathcal{L}_M^{\rm kin} - V_M - V_{\rm SB} + V_{\rm Anom}, \tag{5}$$

where

$$\mathcal{L}_M^{\rm kin} = \tfrac{1}{4}\,{\rm tr}[\partial_\mu \Phi \partial^\mu \Phi^\dagger], \tag{6}$$

$$V_M = -\tfrac{1}{4}\bar{\mu}^2\,{\rm tr}[\Phi\Phi^\dagger] + \tfrac{1}{8}\lambda_4\,{\rm tr}[(\Phi\Phi^\dagger)^2] - \tfrac{1}{12}\lambda_6\,{\rm tr}[(\Phi\Phi^\dagger)^3] + \lambda_8\,{\rm tr}[(\Phi\Phi^\dagger)^4] + \lambda_{10}\,{\rm tr}[(\Phi\Phi^\dagger)^5], \tag{7}$$

$$V_{\rm SB} = -\tfrac{1}{2}c\,{\rm tr}[\mathcal{M}^\dagger\Phi + \mathcal{M}\Phi^\dagger], \tag{8}$$

$$V_{\rm Anom} = -B[\det\Phi + \det\Phi^\dagger]. \tag{9}$$

Here B is the coefficient for the axial anomaly term and c is the coefficient for the explicit chiral symmetry-breaking term with $\mathcal{M}$ defined as $\mathcal{M} = {\rm diag}\{m_u, m_d, m_s\}$. The above Lagrangian for the meson part is $U(1)_A$ invariant except the anomaly term. We note that we include only terms with one trace in V_M, which are expected to be of leading order in the $1/N_c$ expansion.

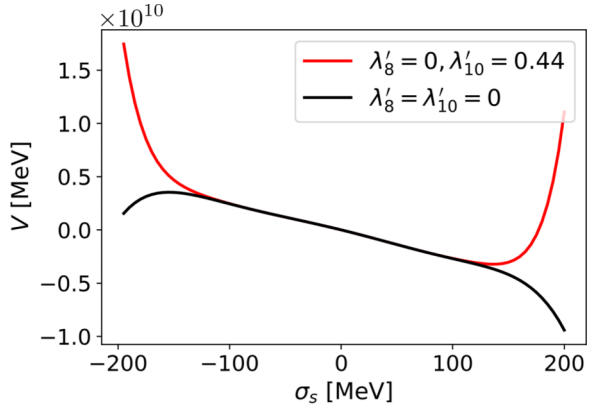

FIG. 2. The potential for σ_s in the vacuum with $m_0 = 800$ MeV; $\lambda_8' = \lambda_8 f_\pi^4$, $\lambda_{10}' = \lambda_{10} f_\pi^6$.

Compared with the previous model in Ref. [36], we not only include the anomaly term but also introduce the λ_8 and λ_{10} terms to stablize the potential in the vacuum. In fact, the σ^6 term is negative, and the potential is unbound at very large σ unless we have higher-order terms. In the previous studies we focused on the local minimum giving $\sigma = f_\pi$, while neglecting unphysical behaviors at large σ where we distrust potentials limited to the σ^6 terms. For three flavors with the 't Hooft term, however, it turns out that the potential is not only unbound for very large σ_s but does not even have a local minimum, see Fig. 2. For this reason we need to fix our descriptions for higher-order terms which we have neglected in our previous studies. In this work we stablize the potential by adding the λ_8 and λ_{10} terms. Two terms are used just for fine tuning purposes.

In this work we use a hadronic model only up to $2n_0$ neglecting hyperons. Within mean-field treatments adopted in this paper, only the diagonal components are kept. So we reduce Φ to

$$\Phi = \begin{pmatrix} M & 0 \\ 0 & \phi_s \end{pmatrix}_{3\times 3}, \tag{10}$$

where we keep the abstract notation M as a 2×2 matrix field to keep track of the SU(2)$_L\times$ SU(2)$_R\times$ U(1)$_A$ structure of our model. The meson field under chiral transformation in the SU(2) case is

$$M \to g_L M g_R^\dagger, \tag{11}$$

where $g_L \in$ SU(2)$_L$ and $g_R \in$ SU(2)$_R$. Then the reduced Lagrangian is

$$\begin{aligned}
\mathcal{L}_M^{\rm scalar} &= \tfrac{1}{4}(\mathrm{tr}[\partial_\mu M \partial^\mu M^\dagger] + \partial_\mu \phi_s \partial^\mu \phi_s^\dagger), \qquad (12)\\
V_M &= -\tfrac{1}{4}\bar{\mu}^2(\mathrm{tr}[MM^\dagger] + \phi_s\phi_s^\dagger) \\
&\quad + \tfrac{1}{8}\lambda_4(\mathrm{tr}[(MM^\dagger)^2] + (\phi_s\phi_s^\dagger)^2) \\
&\quad - \tfrac{1}{12}\lambda_6(\mathrm{tr}[(MM^\dagger)^3] + (\phi_s\phi_s^\dagger)^3) \\
&\quad + \lambda_8(\mathrm{tr}[(MM^\dagger)^4] + (\phi_s\phi_s^\dagger)^4) \\
&\quad + \lambda_{10}(\mathrm{tr}[(MM^\dagger)^5] + (\phi_s\phi_s^\dagger)^5), \qquad (13)
\end{aligned}$$

$$V_{\rm SB} = -\frac{c}{2}[\mathrm{tr}[\mathcal{M}_{2\times 2}(M + M^\dagger)] + m_s(\phi_s + \phi_s^\dagger)], \tag{14}$$

$$V_{\rm Anom} = -B[\det(M)\phi_s + \det(M^\dagger)\phi_s^\dagger]. \tag{15}$$

where $\mathcal{M}_{2\times 2} = \mathrm{diag}\{m_u, m_d\}$.

B. Nucleon parity doublet and vector mesons

While we treat the mesonic sector including three-flavors, we discuss nucleons only up to $2n_0$ where we assume that hyperons do not enter the system. In the PDM, we assume that nucleons and the chiral partners belong to the representations of $(\mathbf{2},\mathbf{1})_{+1}$ and $(\mathbf{1},\mathbf{2})_{-1}$ as

$$\psi_1^L : (\mathbf{2},\mathbf{1})_{-1}, \quad \psi_1^R : (\mathbf{1},\mathbf{2})_{+1}, \tag{16}$$

$$\psi_2^L : (\mathbf{1},\mathbf{2})_{+1}, \quad \psi_2^R : (\mathbf{2},\mathbf{1})_{-1}, \tag{17}$$

under SU(2)$_L\times$ SU(2)$_R\times$ U(1)$_A$ symmetry. In mean-field treatments, these fields couple to the two-flavor part in the three-flavor mesonic Lagrangian. Then the nucleon part constructed based on the SU(2)$_R\times$ SU(2)$_L\times$ U(1)$_A$ symmetry is given by

$$\begin{aligned}
\mathcal{L}_N = &\sum_{i=1,2} \bar{\psi}_i i\gamma^\mu D_\mu \psi_i \\
&- g_1\left[\bar{\psi}_1^L \tau^2 (M^\dagger)^T \tau^2 \psi_1^R + \bar{\psi}_1^R \tau^2 M^T \tau^2 \psi_1^L\right] \\
&- g_2\left[\bar{\psi}_2^L \tau^2 M^T \tau^2 \psi_2^R + \bar{\psi}_2^R \tau^2 (M^\dagger)^T \tau^2 \psi_2^L\right] \\
&- m_0\left(\bar{\psi}_1^L \psi_2^R - \bar{\psi}_1^R \psi_2^L - \bar{\psi}_2^L \psi_1^R + \bar{\psi}_2^R \psi_1^L\right),
\end{aligned} \tag{18}$$

where $\tau_i (i = 1, 2, 3)$ are the Pauli matrices. The couplings $g_{1,2}$ are the Yukawa couplings to the scalar fields for $\psi_{1,2}$ and the origin of the chiral variant masses. Meanwhile m_0 is the chiral invariant mass which originate from the coupling between ψ_1 and ψ_2. In the mean-field treatment of σ, the mass spectra are given by

$$m_\pm = \sqrt{m_0^2 + \left(\frac{g_1 + g_2}{2}\right)^2 \sigma^2} \mp \frac{g_1 - g_2}{2}\sigma, \tag{19}$$

where $+$ is for $N(940)$ and $-$ for $N(1535)$ as the mixture of ψ_1 and ψ_2 fields. For vanishing σ, the masses get degenerated, $m_\pm \to m_0$.

The coupling of vector mesons to nucleons is introduced in the form of the covariant derivatives

$$D_\mu \psi_{1,2}^{L,R} = (\partial_\mu - iV_\mu)\psi_{1,2}^{L,R}. \tag{20}$$

with V_μ general external fields including ω and ρ mesons coupled to baryon number and isospin densities, respectively.

The Lagrangian for vector mesons is based on the hidden local symmetry (HLS) [47,48]. This part is not affected by the U(1)$_A$ anomaly. We use the same form as the previous works except addition of the following term:

$$\mathcal{L}_{\omega\rho} = \lambda_{\omega\rho}(g_\omega \omega)^2 (g_\rho \rho)^2, \tag{21}$$

where $\lambda_{\omega\rho}$ is assumed to be positive, meaning the attractive correlation between the ω and ρ fields. This term assists the appearance of ρ fields as ω fields develop. The ω-ρ correlations play important roles in the symmetry energy, as will be discussed in the following section.

III. NUCLEAR AND QUARK EQUATIONS OF STATE

In this section, we construct neutron star matter EOS in both hadronic matter part and quark matter part.

A. Nuclear matter EOS

Following Ref. [36], we apply the mean-field approximation to the Lagrangian in the last section, and then calculate the thermodynamic potential in the hadronic matter as

$$\begin{aligned}\Omega_{\rm PDM} &= V(\sigma,\sigma_s) - V(\sigma_0,\sigma_{s0}) - \frac{1}{2}m_\omega^2\omega^2 - \frac{1}{2}m_\rho^2\rho^2 \\ &- \lambda_{\omega\rho}(g_\omega\omega)^2(g_\rho\rho)^2 \\ &- 2\sum_{i=+,-}\sum_{\alpha=p,n}\int^{k_f}\frac{d^3\mathbf{p}}{(2\pi)^3}\left(\mu_\alpha^* - E_p^i\right). \end{aligned} \tag{22}$$

Here $i=+,-$ denote for the parity of nucleons and $E_{\mathbf{p}}^i = \sqrt{\mathbf{p}^2+m_i^2}$ is the energy of nucleons with mass m_i and momentum $\mathbf{p}$. The crossing term ω-ρ interaction is tuned to adjust the slope parameter, see Sec. IV. The potential $V(\sigma,\sigma_s)$ of σ and σ_s mean fields is given by

$$\begin{aligned}V(\sigma,\sigma_s) &= -\frac{1}{2}\bar{\mu}^2\left(\sigma^2+\frac{1}{2}\sigma_s^2\right) + \frac{1}{4}\lambda_4\left(\sigma^4+\frac{1}{2}\sigma_s^4\right) \\ &- \frac{1}{6}\lambda_6\left(\sigma^6+\frac{1}{2}\sigma_s^6\right) + \lambda_8\left(2\sigma^8+\sigma_s^8\right) \\ &+ \lambda_{10}\left(2\sigma^{10}+\sigma_s^{10}\right) - 2B\sigma^2\sigma_s \\ &- (2cm_u\sigma + cm_s\sigma_s). \end{aligned} \tag{23}$$

The total thermodynamic potential for the NS is obtained by including the effects of leptons as

$$\Omega_H = \Omega_{\rm PDM} + \sum_{l=e,\mu}\Omega_l, \tag{24}$$

where $\Omega_l(l=e,\mu)$ are the thermodynamic potentials for leptons,

$$\Omega_l = -2\int^{k_F}\frac{d^3\mathbf{p}}{(2\pi)^3}\left(\mu_l - E_{\mathbf{p}}^l\right). \tag{25}$$

The mean fields here are determined by following stationary conditions:

$$0 = \frac{\partial\Omega_H}{\partial\sigma}, \quad 0 = \frac{\partial\Omega_H}{\partial\omega}, \quad 0 = \frac{\partial\Omega_H}{\partial\rho}. \tag{26}$$

We also need to impose the β equilibrium and the charge neutrality conditions,

$$\mu_e = \mu_\mu = -\mu_Q, \tag{27}$$

$$\frac{\partial\Omega_H}{\partial\mu_Q} = n_p - n_l = 0, \tag{28}$$

where μ_Q is the charge chemical potential. We then have the pressure in hadronic matter as

$$P_H = -\Omega_H. \tag{29}$$

B. Quark matter EOS

Following Refs. [2,49], we use the NJL quark model to describe the quark matter. The model includes three-flavors and $U(1)_A$ anomaly effects through the quark version of the KMT interaction. The coupling constants are chosen to be the Hatsuda-Kunihiro parameters which successfully reproduce the hadron phenomenology at low energy [2,50]: $G\Lambda^2 = 1.835$, $K\Lambda^5 = 9.29$, with $\Lambda = 631.4$ MeV, see the definition below. The couplings g_V and H characterize the strength of the vector repulsion and attractive diquark correlations whose range will be examined later when we discuss the NS constraints.

We can then write down the thermodynamic potential as

$$\begin{aligned}\Omega_{\rm CSC} &= \Omega_s - \Omega_s\left[\sigma_f = \sigma_f^0, d_j = 0, \mu_q = 0\right] \\ &+ \Omega_c - \Omega_c\left[\sigma_f = \sigma_f^0, d_j = 0\right], \end{aligned} \tag{30}$$

where the subscript 0 is attached for the vacuum values, and

$$\Omega_s = -2\sum_{i=1}^{18}\int^{\Lambda}\frac{d^3\mathbf{p}}{(2\pi)^3}\frac{\epsilon_i}{2}, \tag{31}$$

$$\Omega_c = \sum_i\left(2G\sigma_i^2 + Hd_i^2\right) - 4K\sigma_u\sigma_d\sigma_s - g_V n_q^2, \tag{32}$$

with σ_f are the chiral condensates, d_j are diquark condensates, and n_q is the quark density. In Eq. (31), ϵ_i are energy eigenvalues obtained from inverse propagator in Nambu-Gorkov bases,

$$S^{-1}(k) = \begin{pmatrix}\gamma_\mu k^\mu - \hat{M} + \gamma^0\hat{\mu} & \gamma_5\sum_i\Delta_i R_i \\ -\gamma_5\sum_i\Delta_i^* R_i & \gamma_\mu k^\mu - \hat{M} - \gamma^0\hat{\mu}\end{pmatrix}, \tag{33}$$

where

$$\begin{aligned}M_i &= m_i - 4G\sigma_i + K\left|\epsilon_{ijk}\right|\sigma_j\sigma_k, \\ \Delta_i &= -2Hd_i, \\ \hat{\mu} &= \mu_q - 2g_V n_q + \mu_3\lambda_3 + \mu_8\lambda_8 + \mu_Q Q, \\ (R_1,R_2,R_3) &= (\tau_7\lambda_7, \tau_5\lambda_5, \tau_2\lambda_2). \end{aligned} \tag{34}$$

$S^{-1}(k)$ is 72×72 matrix in terms of the color, flavor, spin, and Nambu-Gorkov basis, which has 72 eigenvalues; $M_{u,d,s}$ are the constituent masses of u,d,s quarks and $\Delta_{1,2,3}$ are the gap energies. The $\mu_{3,8}$ are the color chemical potentials which will be tuned to achieve the color neutrality. The total thermodynamic potential including the effect of leptons is

$$\Omega_Q = \Omega_{\rm CSC} + \sum_{l=e,\mu}\Omega_l. \tag{35}$$

The mean fields are determined from the gap equations,

$$0 = \frac{\partial\Omega_Q}{\partial\sigma_i} = \frac{\partial\Omega_Q}{\partial d_i}. \tag{36}$$

From the conditions for electromagnetic charge neutrality and color charge neutrality, we have

$$n_j = -\frac{\partial\Omega_Q}{\partial\mu_j} = 0, \tag{37}$$

TABLE I. Physical inputs in vacuum in unit of MeV.

m_π	m_K	f_π	f_K	m_ω	m_ρ	m_+	m_-
140	494	92.4	109	783	776	939	1535

where $j = 3, 8, Q$. The baryon number density n_B is determined as

$$n_q = -\frac{\partial \Omega_Q}{\partial \mu_q}, \tag{38}$$

where μ_q is 1/3 of the baryon number chemical potential. After determined all the values, we obtain the pressure as

$$P_Q = -\Omega_Q. \tag{39}$$

IV. PARAMETER DETERMINATION

In this section, we determine the parameters in the PDM by fitting with the normal nuclear matter properties and the decay constants for different m_0 (summarized in Table I and Table II). It is notified that, for $B = \lambda_8 = \lambda_{10} = 0$, the present model is exactly the same as Refs. [34,36] and the model parameters can be determined in the same way. As in the previous works, we use the vector masses $m_\rho = 776$ MeV and $m_\omega = 783$ MeV. The parameters $cm_u = cm_d$ and cm_s are fixed by the following relations with f_π and f_K given in Table I,

$$2cm_u = m_\pi^2 f_\pi^2, \quad c(m_u + m_s) = m_K^2 f_K^2. \tag{40}$$

We are left with 11 parameters which will be tuned in the presence of the U(1)$_A$ anomaly. The mesonic part contains

$$\bar{\mu}^2,\ \lambda_4,\ \lambda_6,\ \lambda_8,\ \lambda_{10},\ B,\ \lambda_{\omega\rho}, \tag{41}$$

and the nucleonic Lagrangian contains

$$m_0,\ g_1,\ g_2,\ g_{\omega NN},\ g_{\rho NN}. \tag{42}$$

In this paper, we treat m_0 as a given input and then fix the other parameters. When we present results for m_0 different from the values in this section, those results are obtained after retuning the above parameters to achieve the same quality of fitting as in the present section, unless otherwise stated.

The mesonic part is constrained by the vacuum physics and nuclear saturation properties. In vacuum, the couplings (g_1, g_2), for a given m_0, are fixed by demanding $m_+^{\rm vac} = 939$ MeV and $m_-^{\rm vac} = 1535$ MeV through the relation,

$$m_\pm^{\rm vac} = \sqrt{m_0^2 + \left(\frac{g_1 + g_2}{2}\right)^2 \sigma_0^2} \mp \frac{|g_1 - g_2|}{2}\sigma_0. \tag{43}$$

TABLE II. Saturation properties used to determine the model parameters: The saturation density n_0, the binding energy B_0, the incompressibility K_0, symmetry energy S_0, and the slope parameter L_0.

n_0 (fm^{-3})	$E_{\rm Bind}$ (MeV)	K_0 (MeV)	S_0 (MeV)	L_0 (MeV)
0.16	16	240	31	57.7

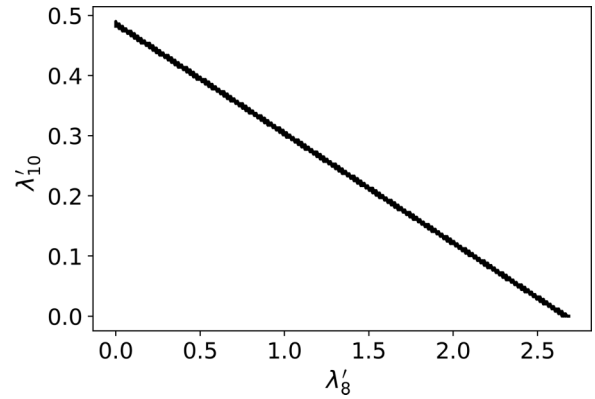

FIG. 3. Restricted combination of λ_8 and λ_{10} after fixing the value of σ_s with $m_0 = 800$ MeV. $\lambda'_8 = \lambda_8 f_\pi^4$, $\lambda'_{10} = \lambda_{10} f_\pi^6$.

where the σ fields in vacuum are given by

$$\sigma_0 = f_\pi, \quad \sigma_{s0} = f_K - \frac{f_\pi}{2}. \tag{44}$$

In order to satisfy these relations on σ_0 and σ_{s0}, a proper range of the mesonic parameters in Eq. (41) must be chosen.

There is still large degeneracy among the mesonic parameters. We can break the degeneracy by demanding the mesonic parameters and $(g_{\omega NN},\ g_{\rho NN},\ \lambda_{\omega\rho})$ to reproduce the saturation properties listed in Table II. Then we are left with the degeneracy related to the choice of parameters λ_8, λ_{10}, and B. We show the degeneracy related to λ_8 and λ_{10} in Fig. 3 by showing the range to reproduce the above-mentioned saturation properties.

Finally, the parameter B is strongly correlated with the η and η' masses whose experimental values in the vacuum are

$$m_\eta^{\rm exp} \simeq 547.9 \text{ MeV}, \quad m_{\eta'}^{\rm exp} \simeq 957.8 \text{ MeV}. \tag{45}$$

We fix the parameters to reproduce the above-mentioned vacuum and saturation properties for a given B. We repeat this procedure while increasing B until the parameters reproduce η and η' masses correctly. The behaviors of η and η' masses as functions of B are displayed in Fig. 4. The width attached

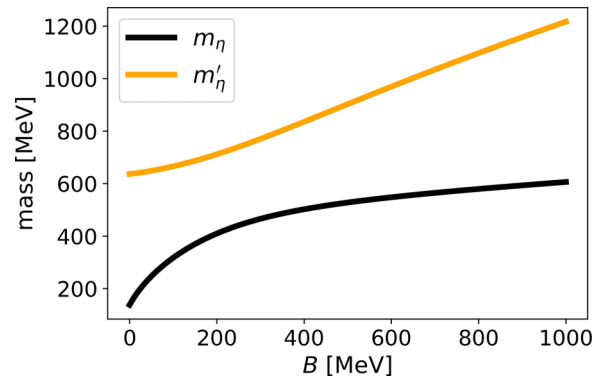

FIG. 4. The B dependence of masses of η and η' mesons in the vacuum with unit MeV.

TABLE III. Values of model parameters determined for several choices of $\lambda_8' = \lambda_8 f_\pi^4$. When $B = 600$ MeV, we only find solutions which satisfy the saturation properties in the range $0 \leqslant \lambda_8' \leqslant 2.64$; here we list the boundary values as a typical example. $\lambda_8' = 0$ is the minimum boundary and $\lambda_8' = 2.64$ is the maximum boundary.

	$m_0 = 800$ (MeV)	$\lambda_8' = 0$	$\lambda_8' = 2.64$
$B = 0$ (MeV)	g_1	6.99	6.99
	g_2	13.4	13.4
	$\bar{\mu}^2/f_\pi^2$	24.83	38.15
	λ_4	63.52	115.27
	$\lambda_6 f_\pi^2$	45.27	117.99
	$\lambda_{\omega\rho}$	0.52	0.69
	$\lambda_{10} f_\pi^6$	0.44	0.04
	$g_{\omega NN}$	5.12	4.85
	$g_{\rho NN}$	10.25	10.27
$B = 600$ (MeV)	g_1	6.99	6.99
	g_2	13.4	13.4
	$\bar{\mu}^2/f_\pi^2$	7.22	25.89
	λ_4	102.8	166.02
	$\lambda_6 f_\pi^2$	66.23	145.23
	$\lambda_{\omega\rho}$	0.66	0.81
	$\lambda_{10} f_\pi^6$	0.44	0.04
	$g_{\omega NN}$	4.17	3.82
	$g_{\rho NN}$	9.31	9.21

to the curves reflects the different combinations of λ_8 and λ_{10}. For $B = 600$ MeV, the masses of η' and η are calculated as

$$m_\eta^{\rm PDM} = 542 \pm 15 \text{ MeV}, \quad m_{\eta'}^{\rm PDM} = 962 \pm 20 \text{ MeV}. \quad (46)$$

In this paper, we take $B = 600$ MeV as the physical value. Table III shows one example for the parameter determination.

V. EFFECT OF ANOMALY IN MESON SECTOR FOR HADRONIC MATTER

To study the effect of the anomaly, we perform linear analysis with respect to the variation of B; we weakly vary the value of B around our physical choice $B = 600$ MeV, leaving the other parameters unchanged. (Within this linear analysis, the results other than $B = 600$ MeV do not satisfy the saturation properties.)

The vacuum value of σ and σ_s change as shown in Fig. 5. The vacuum values of σ and σ_s increase as B does. This indicates that the anomaly enhances the chiral symmetry breaking, as discussed in the previous sections. The energy density in vacuum is reduced more by the stronger chiral symmetry breaking. When the chiral symmetry is restored, this energy reduction in vacuum is lost, and we have to add more energy density or a *bag constant* to the EOS in the chiral restored phase.

Another important effect of the anomaly is the increase of σ meson mass, as shown in Fig. 6. In the context of nuclear forces, the heavier σ meson mass reduces the range of attractive force and weakens the overall strength; this in turn requires weaker repulsive ω interactions to balance with the σ attraction to satisfy the saturation properties. The resultant reduced repulsion leads to a softer nuclear EOS at suprasaturation densities where ω dominates over σ. In summary, the $U(1)_A$ anomaly effects softens nuclear EOS at suprasaturation densities.

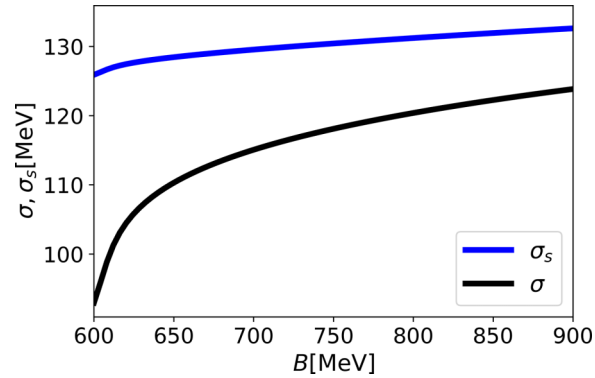

FIG. 5. The B dependence of σ and σ_s for $m_0 = 500$ MeV.

In Fig. 7, we show the density dependence of the energy density for $B = 580$, 600, and 620 MeV with $m_0 = 800$ MeV. The energy density overall increases as B does in whole density region, and the saturation points shift to higher densities. This can be understood by the competition between the σ attraction and ω repulsion. In the present linear analyses, increasing B does not change the vector meson mass but increases the mass of σ. As a result, the range of σ attraction, $\approx 1/m_\sigma$, decreases as B increases, reducing the attractive contributions to the energy density. We also show the energy dependence of the pressure in the Fig. 8 is obtained through

$$P = \mu_B n_B - \varepsilon, \quad (47)$$

which indicates that the effect of anomaly softens the equation of state.

VI. EFFECT OF ANOMALY IN NJL-TYPE MODEL FOR QUARK MATTER

In the NJL-type model introduced in Sec. III B, the coefficient K represents the strength of anomaly. Here we gradually decrease the value of K from $K\Lambda^5 = 9.29$ toward 0 with fixing other parameters to study the effect of anomaly. For simplicity, we first set $H = 0$ to avoid diquark condensate.

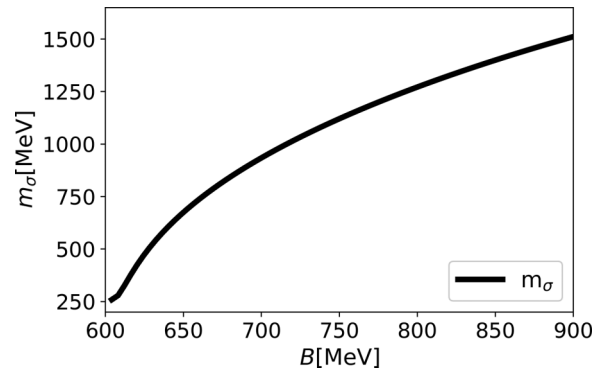

FIG. 6. The B dependence of m_σ for $m_0 = 500$ MeV.

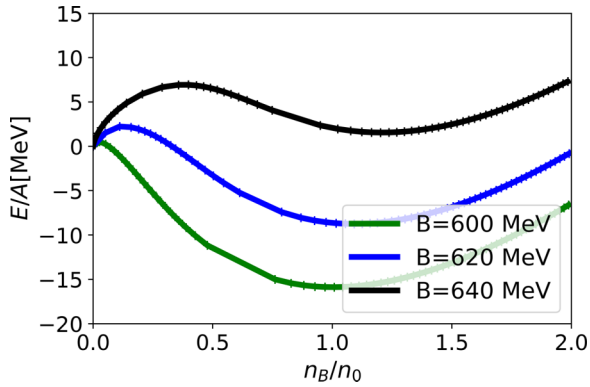

FIG. 7. Density dependence of the energy for $m_0 = 500$ MeV.

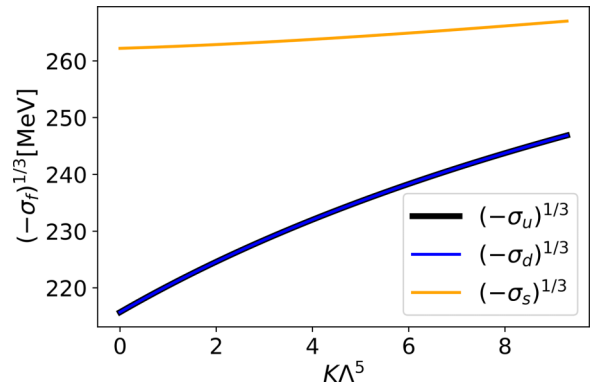

FIG. 9. The dependence of chiral condensates on the value of K. The horizontal axis shows the value of K normalized as $K\Lambda^5$.

The chiral condensates in the vacuum have the anomaly dependence as in Fig. 9.

Chiral condensates in vacuum increase with increasing K, which is similar to the PDM. This result indicates that the anomaly enhances the chiral symmetry breaking and reduces the ground-state energy in vacuum.

In Fig. 1 we show dispersion relations of quarks in the chiral symmetry broken vacuum (left panel) and in the chiral symmetric vacuum (right panel). The approximate chiral symmetry is spontaneously broken by the chiral condensate, and quarks of different chiralities are connected with each other. Then the condensation opens a gap M in the quark dispersion relation. As a result, the structure of the Dirac sea is changed to generate a nonperturbative QCD vacuum. The difference in energy density between the chiral symmetric Dirac sea and symmetry-broken Dirac sea defines the bag constant [51],

$$\varepsilon_{\rm bag} = \varepsilon(M_{\rm eff} = m_q) - \varepsilon(M_{\rm eff} = M), \tag{48}$$

where $M_{\rm eff}$ is the effective mass of quarks, m_q is the bare quark mass, and M is the constituent quark mass.

The density dependence of $\varepsilon_{\rm total}$ and $\varepsilon_{\rm bag}$ are calculated separately as shown in the Fig. 10 for two cases, $K = 0$ and $K = 9.29/\Lambda^5$. This indicates that $\varepsilon_{\rm bag} > \varepsilon_{\rm bag}^{K=0}$ at the same density, which implies that the effect of anomaly enhances the bag constant and finally increases the total energy.

From the analysis of the chiral condensates in the vacuum in Fig. 9, the anomaly effect lowers the ground-state energy of the vacuum. In Fig. 1, we show a schematic view of vacuum structure. The released energy after chiral symmetry restoration is larger with anomaly than without it, and then at the same density $\varepsilon_{\rm bag} > \varepsilon_{\rm bag}^{K=0}$.

We also calculate the density dependence of the relevant pressures in Fig. 11, where $P_{\rm bag}$ is calculated from $\varepsilon_{\rm bag}$ using the thermodynamic relation,

$$P_{\rm bag} = -\varepsilon_{\rm bag} + \mu_q n_q. \tag{49}$$

This shows that for same density, $P_{\rm total} < P_{\rm total}^{K=0}$, which is mainly caused by the difference of $P_{\rm bag}$, In summary, at a given density

$$\varepsilon_{\rm total} > \varepsilon_{\rm total}^{K=0}, \quad P_{\rm total} < P_{\rm total}^{K=0}, \tag{50}$$

so EOS with a positive K is softer, i.e., P is smaller at a given ε, as shown in Fig. 12.

VII. STUDY OF PROPERTIES OF NS

In this section, following Ref. [36] we construct a unified EOS by connecting the EOS obtained in the PDM introduced in Sec. III A and the EOS of NJL-type quark model given in Sec. III B and solve the TOV equation [52,53] to obtain the NS mass-radius (M-R) relation. As for the interplay between nuclear and quark matter EOS, see, e.g., Ref. [54] for a quick review that classifies types of the interplay.

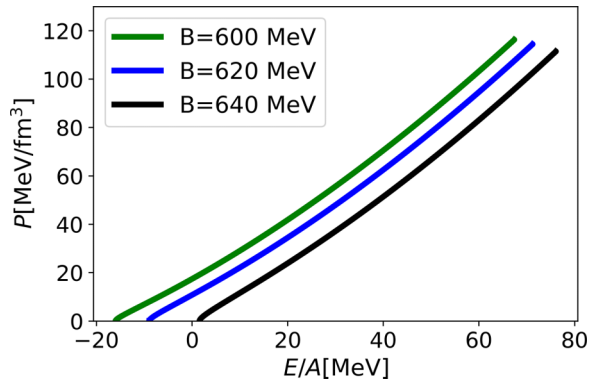

FIG. 8. The energy dependence of pressure for $m_0 = 500$ MeV.

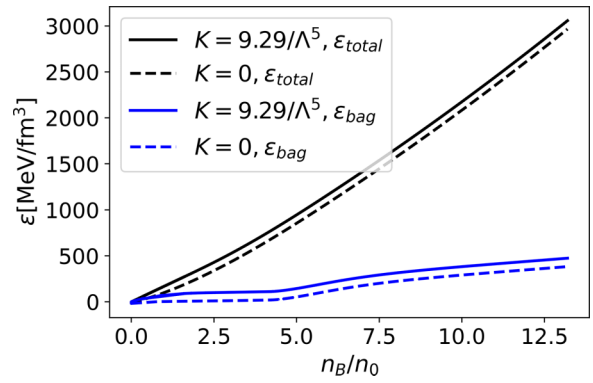

FIG. 10. The density dependence of $\varepsilon_{\rm total}$ and $\varepsilon_{\rm bag}$ with $(H, g_V)/G = (0, 0.1)$.

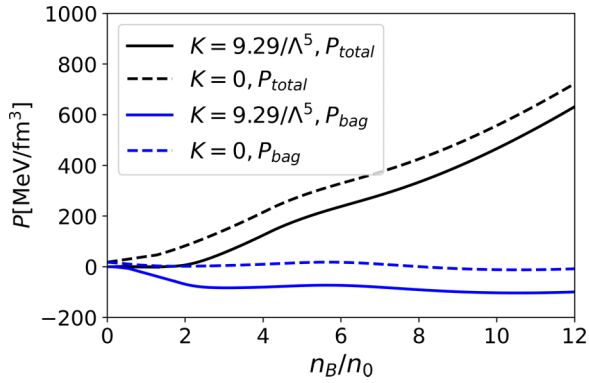

FIG. 11. Density dependence of $P_{\rm total}$ and $P_{\rm bag}$ with $(H, g_V)/G = (0, 0.1)$.

A. Construction of unified EOS

In our unified equations of state as in Table IV, we use the Baym-Pethick-Sutherland EOS [55] as a crust EOS for $n_B \lesssim 0.5n_0$. From $n_B \simeq 0.5n_0$ to $2n_0$ we use our PDM model to describe a nuclear liquid. We limit the use of our PDM up to $2n_0$ so that baryons other than ground-state nucleons, such as the negative parity nucleons or hyperons, do not show up in matter. Beyond the nuclear regime, we assume a crossover from the nuclear matter to quark matter and use a smooth interpolation to construct the unified EOS. We expand the pressure as a fifth-order polynomial of μ_B as

$$P_I(\mu_B) = \sum_{i=0}^{5} C_i \mu_B^i, \tag{51}$$

where C_i $(i = 0, \ldots, 5)$ are parameters to be determined from boundary conditions given by

$$\left.\frac{d^n P_I}{(d\mu_B)^n}\right|_{\mu_{BL}} = \left.\frac{d^n P_H}{(d\mu_B)^n}\right|_{\mu_{BL}},$$
$$\left.\frac{d^n P_I}{(d\mu_B)^n}\right|_{\mu_{BU}} = \left.\frac{d^n P_Q}{(d\mu_B)^n}\right|_{\mu_{BU}}, \quad (n = 0, 1, 2), \tag{52}$$

with μ_{BL} being the chemical potential corresponding to $n_B = 2n_0$ and μ_{BU} to $n_B = 5n_0$. That is, we demand the matching up

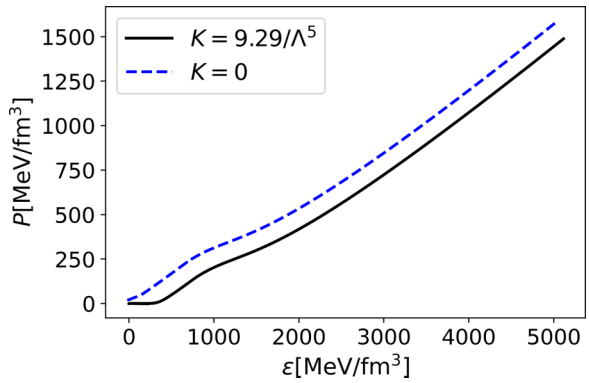

FIG. 12. The energy dependence of pressure for $H/G = 0$, $g_V/G = 0.1$.

TABLE IV. Unified EOS composed of four part

$0 \leqslant n_B < 0.5n_0$	$0.5n_0 \leqslant n_B \leqslant 2n_0$	$5n_0 < n_B < 2n_0$	$n_B \geqslant 5n_0$
Crust	PDM	Interpolation	NJL

to the second-order derivatives of pressure at each boundary. The resultant interpolated EOS must satisfy the thermodynamic stability condition,

$$\chi_B = \frac{\partial^2 P}{(\partial \mu_B)^2} \geqslant 0, \tag{53}$$

and the causality condition,

$$c_s^2 = \frac{dP}{d\varepsilon} = \frac{n_B}{\mu_B \chi_B} \leqslant 1, \tag{54}$$

which means that the sound velocity is less than the light velocity. These conditions restrict the range of quark model parameters (g_V, H) for a given nuclear EOS and a choice of (n_L, n_U).

We exclude interpolated EOSs which do not satisfy the above-mentioned constraints. Similar surveys for the range of (g_V, H) and (n_L, n_U) have been carried out first for APR EOS [56] in Refs. [51,57], and more systematically for Togashi EOS [58] in Ref. [49] and for ChEFT EOS [59] in Ref. [60]. The range explored in the present work is largely consistent with the previous works using different nuclear EOSs. Finally, we note that the estimate based on nonpetrubative massive gluon exchanges favor the estimate of $g_V \approx G$ and $H \approx 1.5G$ [61].

It is important to note that the constraints become severer for the combination of softer nucleonic EOS and stiffer quark EOS. The rapid growth of the stiffness, together with the requirement of $c_s^2 \to 1/3$ in the high-density limit, generally leads to a peak in the sound velocity, as first found phenomenologically in Refs. [39,40] and later explained microscopically in Refs. [62,63] with the emphasis on the quark degrees of freedom. The growth of the stiffness in the crossover model is in general quicker than in purely hadronic models, and such features may be studied in gravitational waves from neutron star merger events [64], or in QCD-like theories, e.g., two-color QCD, for which analytical [65] and lattice calculations [66] suggest the rapid stiffening in the crossover domain.

B. Mass-radius relation

In this section, we study the M-R relations of NSs from the unified EOS constructed above. In Ref. [36], where the anomaly in the nuclear EOS is neglected, the chiral invariant mass is constrained to be 600 MeV $\lesssim m_0 \lesssim$ 900 MeV. In the present analysis, we improve the analyses in three aspects: (i) We include the anomaly in the nuclear EOS, (ii) we newly include the $\omega^2\rho^2$ term for flexible tuning of the slope parameter L in the symmetry energy (here we adopt the value $L = 57.7$ MeV as a baseline suggested by Ref. [67]), and (iii) we include a new constraint from the NICER on the radius of $2.1M_\odot$ neutron stars.

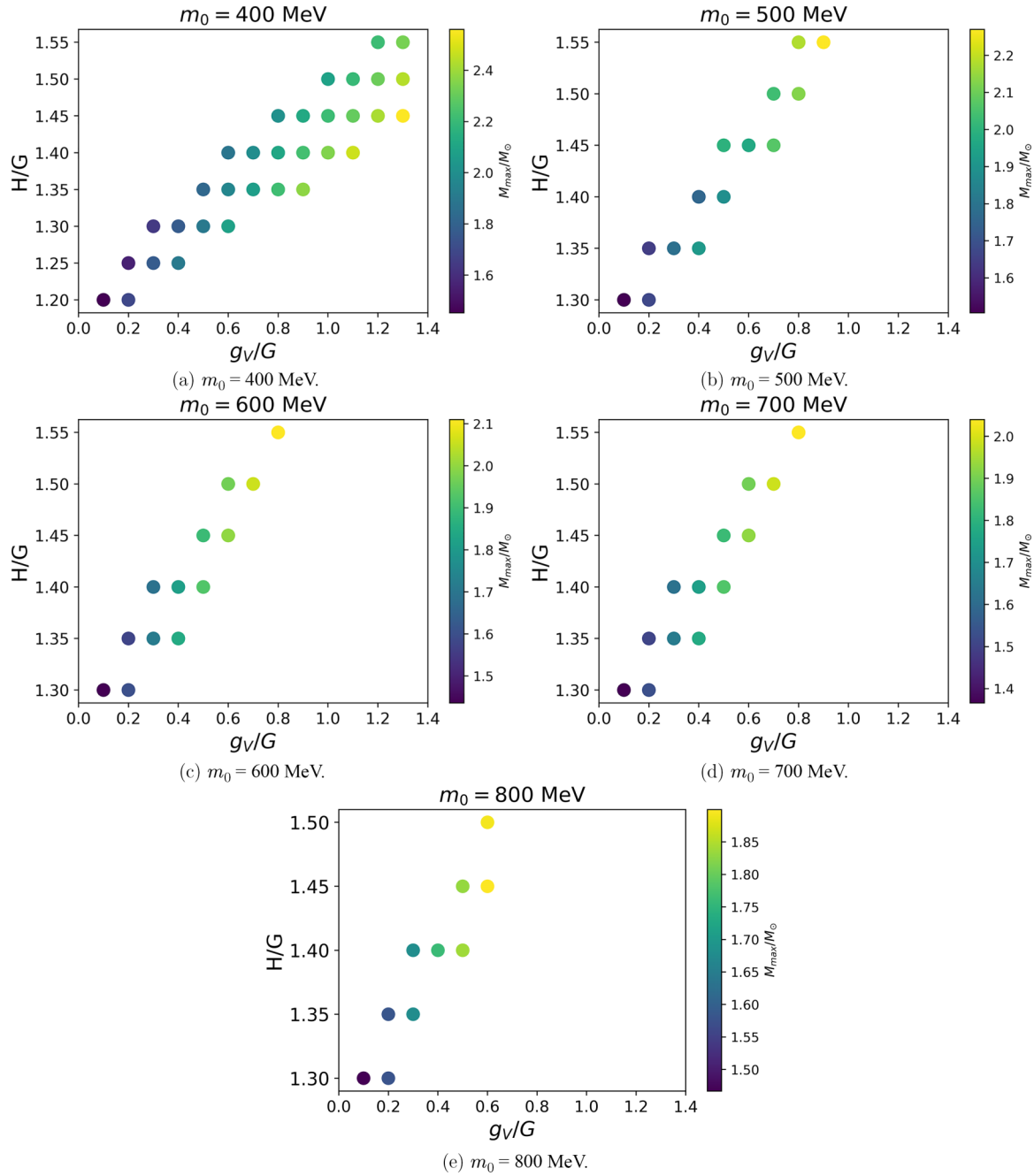

(a) $m_0 = 400$ MeV. (b) $m_0 = 500$ MeV.

(c) $m_0 = 600$ MeV. (d) $m_0 = 700$ MeV.

(e) $m_0 = 800$ MeV.

FIG. 13. Allowed combinations of $(g_V, H)/G$ values for different m_0 choices. The circles indicate that the combinations are allowed and other regions are excluded by the causality condition. The color of the circle shows the maximum mass of NS obtained from the corresponding parameters setting.

We first examine the effects of the NJL parameters (g_V, H). For simplicity, we fix parameters in the PDM to $B = 600$ MeV, $\lambda_8' = 0$, $\lambda_{10}' = 0.44$, and tune $\lambda_{\omega\rho}$ to reproduce $L = 57.7$ MeV. We then vary the value of m_0 and examine the range of (H, g_V) which is allowed by the causality and thermodynamic stability conditions. The band shown in the Fig. 13 specifies such domains, while the blank part is not allowed. A larger g_V requires a larger H. For $m_0 = 800$ MeV, the maximum masses for all the combinations are below $2M_\odot$, leading to the conclusion that $m_0 = 800$ MeV should be excluded within the current setup of the PDM parameters.

Next we fix $m_0 = 500$ MeV and vary the value of $\lambda_{\omega\rho}$ or L while the rest of hadronic parameters is kept unchanged. The resultant M-R relation is shown in Fig. 14, thick curves in the low (high)-mass region indicate the central density of the NS is smaller than $2n_0$ (larger than $5n_0$), and the NS is made from hadronic matter (quark matter). The thin curves on the other hand show that the core is in the crossover region. From the figure one sees that the EOSs are softened by the effect of the $\omega^2\rho^2$ term and the radius for $L = 57.7$ MeV, $M \simeq 1.4M_\odot$ is about 11.2 km in comparison with the result of $L = 80$ MeV about 12.1 km. There is still a large ambiguity about the

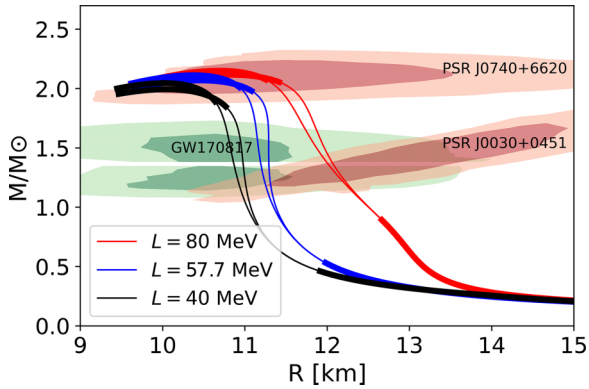

FIG. 14. Mass-radius relations for $m_0 = 500$ MeV with different slope parameter. Red curves are connected to the NJL parameters $(H, g_V)/G = (1.55, 1.0), (1.5, 0.9)$; blue curves to (1.55, 0.9), (1.5, 0.8); black curves to (1.55, 0.8), (1.5, 0.7).

values of slope parameter and small slope parameters usually soften the NS EOS, shifting the radius toward smaller values. Precise determination of slope parameter in the future will help us further constrain the NS properties.

In following analysis, we fix the value $L = 57.7$ MeV and examine the effects of anomaly on the M-R relation. In Fig. 15(a), we show how the M-R curves change under the B effect. The $(\lambda_8', \lambda_{10}')$ parameters from $m_0 = 400$ to 800 MeV are fixed to the boundary values in the following analysis, $\lambda_8' = 0$ and $\lambda_{10}' = 0.44$. The NJL parameter (H, g_V) are chosen to have the stiffest two M-R curves. In the Fig. 15(a), because of the softening effect of the anomaly, after we set $B = 600$ MeV, the stiffest connection for $m_0 = 800$ MeV is unable to satisfy the maximum constraints. In Fig. 15(b), we show the final results in this work after setting $B = 600$ MeV for different m_0 values. We find the final constraints to the chiral invariant mass is changed to be smaller by ≈100 MeV in comparison with the previous constraints in Ref. [36].

VIII. SUMMARY AND DISCUSSION

In this work, we construct an effective hadronic model in which the effect of strange quark condensate is included in the mesonic sector through the KMT-type interaction reflecting the $U(1)$ axial anomaly. We then study the impact of $U(1)_A$ anomaly on the chiral symmetry breaking in both hadronic and an NJL-type quark modes. In both models the $U(1)_A$ anomaly enhances the chiral symmetry breaking. In the PDM, the anomaly effects increases the effective mass of σ, and the heavier σ meson mass reduces the range of attractive force, weakening the overall strength; this in turn requires weaker repulsive ω interactions to balance with the σ attraction to satisfy the saturation properties. The resultant reduced repulsion leads to a softer nuclear EOS at suprasaturation densities. In the NJL-type model, the anomaly effects lead to a large bag constant. Since a larger bag constant adds the energy density but reduces the pressure, the corresponding EOS is softened. We expect that it is a general feature that $U(1)_A$ anomaly softens the NS EOS.

More details about the chiral restoration at finite density are examined in Appendix A for the chiral condensates and in Appendix B for the σ and η' meson masses.

The EOS plays an essential role when determining the NS properties. The NICER analyses of the most massive NS known, PSR J0740+6620, with $M/M_\odot = 2.08 \pm 0.07$ and the radii $R_{2.08} = 12.35 \pm 0.75$ km [45], together with the updated estimate for $R_{1.4} = 12.35 \pm 0.75$ km [45], disfavors strong first-order phase transitions in the region between $1.4M_\odot$ and $2.1M_\odot$.

In this case, we assume the hadronic and quark matter are not distinctly different and construct unified EOS for neutron star matter. In the present work, we interpolate the EOS obtained in the hadronic model based on the parity doublet structure ($n_B \leqslant 2n_0$) and the one in the NJL-type quark model ($n_B \geqslant 5n_0$) with crossover in the intermediate region. We found that the unified EOS is also softened by the effect of anomaly due to the softening of the EOS in both hadronic and quark matters. The resultant M-R curves are compared

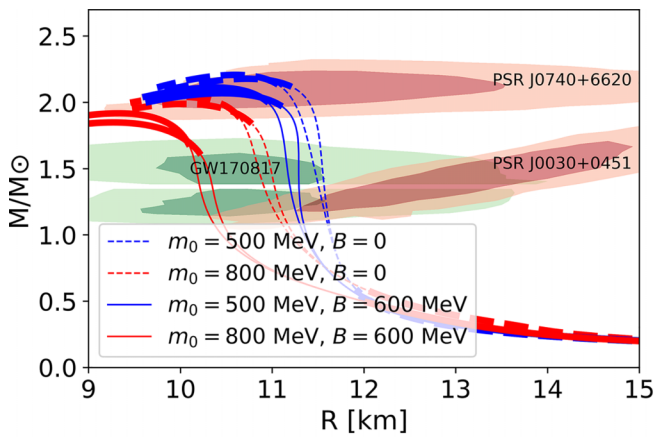

(a) $B = 0$; 600 MeV for $m_0 = 500$; 800 MeV.

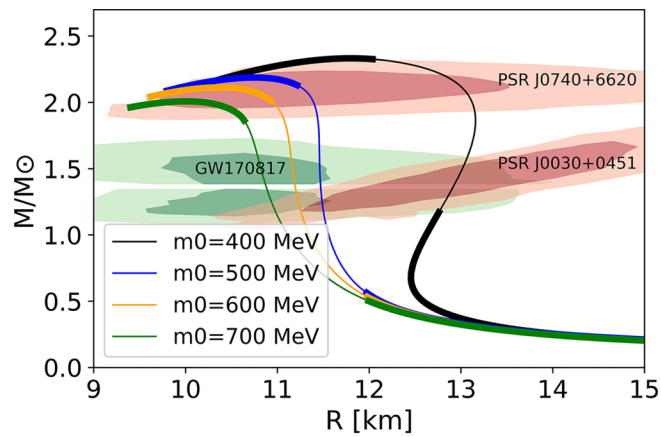

(b) $B = 600$ MeV for different m_0. NJL parameters $(H; gV) / G$ are chosen to be $(1.45,1.3)m_{0=400\text{MeV}}$, $(1.6,1.3)m_{0=500\text{MeV}}$, $(1.6,1.3)m_{0=600\text{MeV}}$, $(1.6,1.2)m_{0=700\text{MeV}}$.

FIG. 15. Mass-radius relations for different m_0 in different parameter setting.

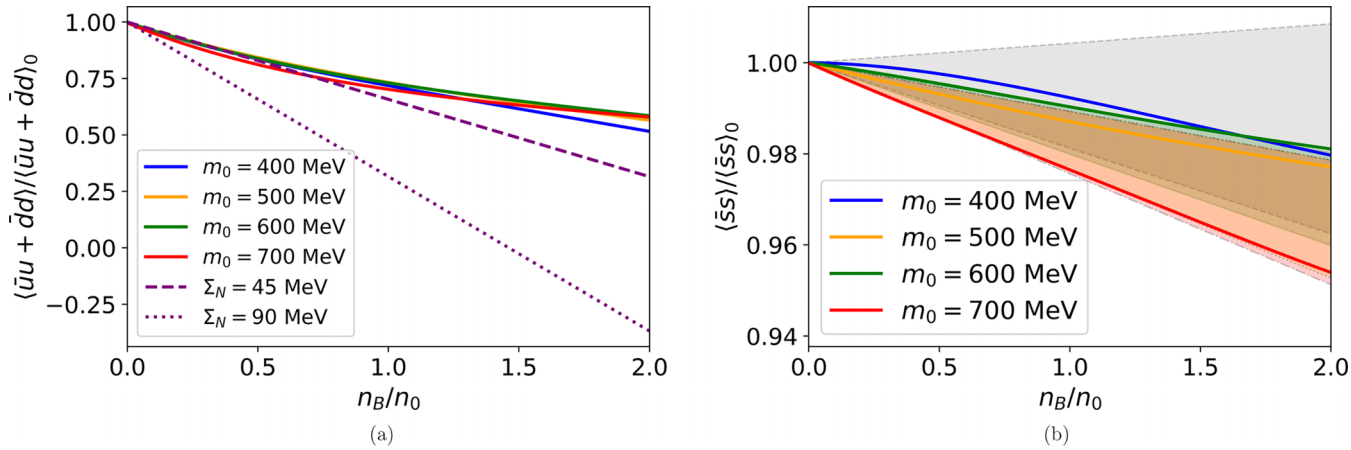

FIG. 16. Density dependence of the chiral condensate $\langle\bar{u}u+\bar{d}d\rangle/\langle\bar{u}u+\bar{d}d\rangle_0$ (left) and $\langle\bar{s}s\rangle/\langle\bar{s}s\rangle_0$ (right) in the PDM. We use the same parameter choices in Fig. 15(b). In (a), two dotted lines show the density dependence in the linear density approximation with $\Sigma_N = 45, 90$ MeV as typical examples. In (b), the colored bands are drawn in the linear density approximation where the value of Σ_{sN} is taken from the lattice QCD results shown in Table V with error bars included: JLQCD (gray band), RQCD (green band), ETM (red band), and χQCD (orange band).

with the constraints from GW170817 (LIGO and VIRGO) and PRS J0030+0451 (NICER) as well as the constraint from PRS J0740+6620. From the constraints we restrict the chiral invariant mass as

$$400\ \text{MeV} \lesssim m_0 \lesssim 700\ \text{MeV}. \tag{55}$$

Compared with results without anomaly, 500 MeV $\lesssim m_0 \lesssim$ 800 MeV, we find that the anomaly softens the EOS, shifting the range of chiral invariant mass toward lower values by 100 MeV. Another new ingredient we added is the $\omega^2\rho^2$ term which is not forbidden by symmetry. Recalling that the role of m_0 is correlated to the balance between σ attraction and ω repulsion, it is also natural to examine the ω-ρ correlations in the context of symmetry energy and then check how it impacts on our previous estimate on m_0. Since the coupling $\lambda_{\omega\rho}$ is strongly correlated with the slope parameter L [68], we show the impact on EOS or M-R relations in Fig. 14 as functions of L. The curves with $L = 80$ MeV corresponds to $\lambda_{\omega\rho} = 0$, and L becomes lower as we increase $\lambda_{\omega\rho}$ (more attractive correlations). The range of $L = 30$–80 MeV [69,70] is the standard.

Small values of L not only decrease the total radius but also lead to smaller maximum mass. Future constraints on L from the experiments will help us to better constrain the values of chiral invariant mass.

In this paper, we included the U(1)$_A$ breaking only in the mesonic sector where the anomaly significantly affects η' mass and the vacuum energy. In the baryonic sector, there may be Yukawa interactions with the U(1)$_A$ breaking, but we are not aware of which part of physics is strongly affected by such terms. Presumably the U(1)$_A$ effects in the Yukawa couplings are largely masked by the uncertainties of those couplings. We leave this problem for future studies. Another important ingredient we omitted is hyperons. We assumed that they do not show up at $n_B \lesssim 2n_0$, but they may still affect the Dirac sea structure by the mass modification through the change of σ and σ_s. We leave these analyses as future works.

ACKNOWLEDGMENTS

The work of B.G., T.M., and M.H. was supported in part by JSPS KAKENHI Grant No. 20K03927. T.M. was also supported by JST SPRING, Grant No. JPMJSP2125 and T.K. by NSFC Grant No. 11875144 and by the Graduate Program on Physics for the Universe at Tohoku University.

APPENDIX A: CHIRAL CONDENSATES

We calculate the chiral condensates in the PDM by differentiating the thermodynamic potential with respect to the current quark masses [11]:

$$\langle(\bar{u}u+\bar{d}d)\rangle \equiv \frac{\partial\Omega_{\text{PDM}}}{\partial m_q}. \tag{A1}$$

Then, using the Gell-Mann-Oakes-Renner relation, we obtain

$$\frac{\langle(\bar{u}u+\bar{d}d)\rangle}{\langle(\bar{u}u+\bar{d}d)\rangle_0} = \frac{\sigma}{f_\pi}. \tag{A2}$$

Similarly, we obtain

$$\langle\bar{s}s\rangle \equiv \frac{\partial\Omega_{\text{PDM}}}{\partial m_s}, \tag{A3}$$

and

$$\frac{\langle\bar{s}s\rangle}{\langle\bar{s}s\rangle_0} = \frac{\sigma_s}{\sigma_{s0}}. \tag{A4}$$

where σ_{s0} is the mean field σ_s at the vacuum.

TABLE V. Values of Σ_{sN} obtained by recent from lattice QCD simulations.

Collaboration	Σ_{sN} (MeV)
χQCD	40.2(11.7)(3.5) [71]
ETM	41.1(8.2)(7.8) [72]
RQCD	35(12) [73]
JLQCD	17(18)(9) [74]

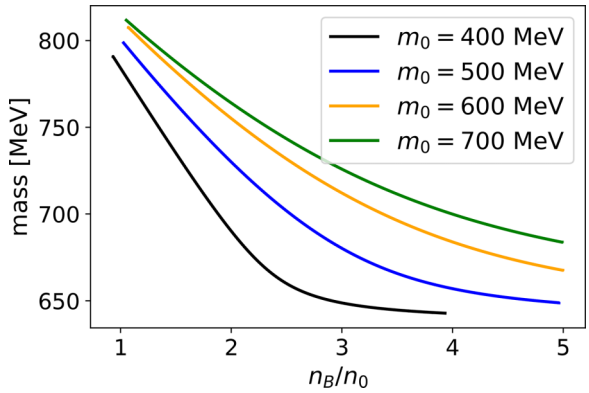

FIG. 17. The density dependence of the η' mass in the PDM for various m_0. The curves are extrapolated from $\leqslant 2n_0$, where we trust the PDM, to higher density.

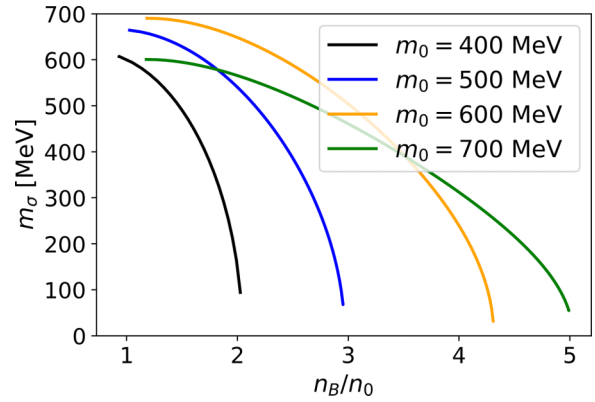

FIG. 18. The density dependence of the effective mass of the σ meson in the PDM for various m_0.

In the linear density approximation, the density dependence of the condensates are given by

$$\langle \bar{q}q \rangle \simeq \langle 0|\bar{q}q|0\rangle + n_B \langle N|\bar{q}q|N\rangle = \langle 0|\bar{q}q|0\rangle + n_B \frac{\Sigma_N}{2m_q}, \quad \text{(A5)}$$

$$\langle \bar{s}s \rangle \simeq \langle 0|\bar{s}s|0\rangle + n_B \langle N|\bar{s}s|N\rangle = \langle 0|\bar{s}s|0\rangle + n_B \frac{\Sigma_{sN}}{m_s}, \quad \text{(A6)}$$

where Σ_N is the πN sigma term and Σ_{sN} is the strange quark sigma term.

In Fig. 16(a), we show the density dependence of $\langle(\bar{u}u + \bar{d}d)\rangle/\langle(\bar{u}u + \bar{d}d)\rangle_0$ determined from the PDM in the neutron star matter. We also plot typical examples of the density dependence of the condensate determined in the linear density approximation where the πN sigma term is taken as $\Sigma_N = 45, 90$ MeV [11]. This shows that in the low-density region, the density dependence of chiral condensate obtained in our model is consistent with the linear density approximation, while there is some deviation in density region $n_B/n_0 \gtrsim 0.5$ due to the higher-order correction.

In Fig. 16(b), we show the density dependence of strange quark chiral condensate compared with the linear density approximation shown by colored bands. In the linear density approximation, we use the value of Σ_{sN} determined by the lattice QCD simulations shown in Table V as typical examples. The colored bands in Fig. 15(b) are written by taking account of all the errors, e.g., $\Sigma_{sN} = 40.2 \pm 15.2$ MeV for χQCD [71]. Figure 16(b) shows that the ambiguity of Σ_{sN} is too large to give a constraint to our model. However, we expect that the precise determination of Σ_{sN} in the future will constrain the chiral invariant mass.

APPENDIX B: MESON MASSES

In addition to the chiral condensates it is useful to examine meson masses at finite density. Here we present the η' and σ meson masses calculated within the PDM.

Shown in Fig. 17 is the η' mass computed in the PDM for various m_0. It drops from $\simeq$960 MeV in vacuum to $\simeq$700–780 MeV at $n_B = 2n_0$. The reduction of the η' mass should be related to the chiral and $U(1)_A$ restoration.

Naïve extrapolation of the PDM result to high density leads to a relatively large η' mass, $\simeq$650–700 MeV at $n_B \simeq 5n_0$ where we expect the presence of quark matter. Meanwhile, the NJL calculations in the CFL quark matter [75–77] suggest a much smaller mass of $\lesssim$100 MeV. Some general formulas and treads have been discussed in Refs. [78–82]. The large mismatch between the PDM extrapolation and quark matter calculations at $5n_0$ suggests that the PDM misses some physics relevant at $\gtrsim 2n_0$. As discussed in Ref. [11], the PDM with a fixed m_0 unlikely describes the modification of the quark Dirac sea and would deviate from predictions based on quark models.

Finally, we also diagnose the density dependence of the σ meson mass, m_σ, for several m_0 as in Fig. 18. For $m_0 = 400$ MeV, the m_σ drops drastically toward $2n_0$. Meanwhile, for a larger m_0, such dropping becomes milder so that conventional nuclear descriptions are rather persistent to $\approx 2n_0$.

[1] S. P. Klevansky, The Nambu-Jona-Lasinio model of quantum chromodynamics, Rev. Mod. Phys. **64**, 649 (1992).
[2] G. Baym, T. Hatsuda, T. Kojo, P. D. Powell, Y. Song, and T. Takatsuka, From hadrons to quarks in neutron stars: A review, Rep. Prog. Phys. **81**, 056902 (2018).
[3] R. S. Hayano and T. Hatsuda, Hadron properties in the nuclear medium, Rev. Mod. Phys. **82**, 2949 (2010).
[4] G. 't Hooft, Symmetry Breaking Through Bell-Jackiw Anomalies, Phys. Rev. Lett. **37**, 8 (1976).
[5] G. 't Hooft, How instantons solve the u(1) problem, Phys. Rep. **142**, 357 (1986).
[6] M. Kobayashi and T. Maskawa, Chiral symmetry and eta-x mixing, Prog. Theor. Phys. **44**, 1422 (1970).
[7] C. DeTar and T. Kunihiro, Linear sigma model with parity doubling, Phys. Rev. D **39**, 2805 (1989).

[8] D. Jido, M. Oka, and A. Hosaka, Chiral symmetry of baryons, Prog. Theor. Phys. **106**, 873 (2001).

[9] G. Aarts, C. Allton, S. Hands, B. Jäger, C. Praki, and J.-I. Skullerud, Nucleons and parity doubling across the deconfinement transition, Phys. Rev. D **92**, 014503 (2015).

[10] T. Yamazaki and M. Harada, Chiral partner structure of light nucleons in an extended parity doublet model, Phys. Rev. D **99**, 034012 (2019).

[11] T. Minamikawa, T. Kojo, and M. Harada, Chiral condensates for neutron stars in hadron-quark crossover: From a parity doublet nucleon model to a Nambu–Jona-Lasinio quark model, Phys. Rev. C **104**, 065201 (2021).

[12] D. Jido, T. Hatsuda, and T. Kunihiro, Chiral Symmetry Realization for Even Parity and Odd Parity Baryon Resonances, Phys. Rev. Lett. **84**, 3252 (2000).

[13] Y. Nemoto, D. Jido, M. Oka, and A. Hosaka, Decays of 1/2-baryons in chiral effective theory, Phys. Rev. D **57**, 4124 (1998).

[14] H. Nishihara and M. Harada, Extended Goldberger-Treiman relation in a three-flavor parity doublet model, Phys. Rev. D **92**, 054022 (2015).

[15] H.-X. Chen, V. Dmitrasinovic, and A. Hosaka, Baryon fields with $U(L)(3) \times U(R)(3)$ chiral symmetry II: Axial currents of nucleons and hyperons, Phys. Rev. D **81**, 054002 (2010).

[16] H.-X. Chen, V. Dmitrasinovic, and A. Hosaka, Baryon fields with $U_L(3) \times U_R(3)$ chiral symmetry III: Interactions with chiral $(3, \bar{3}) + (\bar{3}, 3)$ spinless mesons, Phys. Rev. D **83**, 014015 (2011).

[17] H.-X. Chen, V. Dmitrasinovic, and A. Hosaka, Baryons with $U_L(3) \times U_R(3)$ chiral symmetry IV: Interactions with chiral (8, 1) $\oplus$ (1, 8) vector and axial-vector mesons and anomalous magnetic moments, Phys. Rev. C **85**, 055205 (2012).

[18] T. Hatsuda and M. Prakash, Parity doubling of the nucleon and first-order chiral transition in dense matter, Phys. Lett. B **224**, 11 (1989).

[19] D. Zschiesche, L. Tolos, J. Schaffner-Bielich, and R. D. Pisarski, Cold, dense nuclear matter in a su(2) parity doublet model, Phys. Rev. C **75**, 055202 (2007).

[20] V. Dexheimer, S. Schramm, and D. Zschiesche, Nuclear matter and neutron stars in a parity doublet model, Phys. Rev. C **77**, 025803 (2008).

[21] C. Sasaki and I. Mishustin, Thermodynamics of dense hadronic matter in a parity doublet model, Phys. Rev. C **82**, 035204 (2010).

[22] C. Sasaki, H. K. Lee, W.-G. Paeng, and M. Rho, Conformal anomaly and the vector coupling in dense matter, Phys. Rev. D **84**, 034011 (2011).

[23] S. Gallas, F. Giacosa, and G. Pagliara, Nuclear matter within a dilatation-invariant parity doublet model: The role of the tetraquark at nonzero density, Nucl. Phys. A **872**, 13 (2011).

[24] J. Steinheimer, S. Schramm, and H. Stöcker, Hadronic su(3) parity doublet model for dense matter and its extension to quarks and the strange equation of state, Phys. Rev. C **84**, 045208 (2011).

[25] W.-G. Paeng, H. K. Lee, M. Rho, and C. Sasaki, Dilaton-limit fixed point in hidden local symmetric parity doublet model, Phys. Rev. D **85**, 054022 (2012).

[26] V. Dexheimer, J. Steinheimer, R. Negreiros, and S. Schramm, Hybrid stars in an su(3) parity doublet model, Phys. Rev. C **87**, 015804 (2013).

[27] W.-G. Paeng, H. K. Lee, M. Rho, and C. Sasaki, Interplay between ω-nucleon interaction and nucleon mass in dense baryonic matter, Phys. Rev. D **88**, 105019 (2013).

[28] A. Mukherjee, J. Steinheimer, and S. Schramm, Higher-order baryon number susceptibilities: Interplay between the chiral and the nuclear liquid-gas transitions, Phys. Rev. C **96**, 025205 (2017).

[29] D. Suenaga, Examination of $N^*(1535)$ as a probe to observe the partial restoration of chiral symmetry in nuclear matter, Phys. Rev. C **97**, 045203 (2018).

[30] Y. Takeda, Y. Kim, and M. Harada, Catalysis of partial chiral symmetry restoration by Δ matter, Phys. Rev. C **97**, 065202 (2018).

[31] A. Mukherjee, S. Schramm, J. Steinheimer, and V. Dexheimer, The application of the quark-hadron chiral parity-doublet model to neutron star matter, Astron. Astrophys. **608**, A110 (2017).

[32] H. Abuki, Y. Takeda, and M. Harada, Dual chiral density waves in nuclear matter, EPJ Web Conf. **192**, 00020 (2018).

[33] M. Marczenko, D. Blaschke, K. Redlich, and C. Sasaki, Parity doubling and the dense-matter phase diagram under constraints from multi-messenger astronomy, Universe **5**, 180 (2019).

[34] Y. Motohiro, Y. Kim, and M. Harada, Asymmetric nuclear matter in a parity doublet model with hidden local symmetry, Phys. Rev. C **92**, 025201 (2015).

[35] T. Yamazaki and M. Harada, Constraint to chiral invariant masses of nucleons from gw170817 in an extended parity doublet model, Phys. Rev. C **100**, 025205 (2019).

[36] T. Minamikawa, T. Kojo, and M. Harada, Quark-hadron crossover equations of state for neutron stars: Constraining the chiral invariant mass in a parity doublet model, Phys. Rev. C **103**, 045205 (2021).

[37] M. Harada and T. Yamazaki, Charmed mesons in nuclear matter based on chiral effective models, in *Proceedings of the 8th International Conference on Quarks and Nuclear Physics (QNP'18)*.

[38] M. Marczenko, D. Blaschke, K. Redlich, and C. Sasaki, Toward a unified equation of state for multi-messenger astronomy, Astron. Astrophys. **643**, A82 (2020).

[39] K. Masuda, T. Hatsuda, and T. Takatsuka, Hadron-quark crossover and massive hybrid stars with strangeness, Astrophys. J. **764**, 12 (2013).

[40] K. Masuda, T. Hatsuda, and T. Takatsuka, Hadron–quark crossover and massive hybrid stars, Progr. Theor. Exp. Phys. **2013**, 073D01 (2013).

[41] H. T. Cromartie *et al.*, Relativistic Shapiro delay measurements of an extremely massive millisecond pulsar, Nat. Astron. **4**, 72 (2019).

[42] B. P. Abbott, Gw170817: Observation of Gravitational Waves from a Binary Neutron Star Inspiral, Phys. Rev. Lett. **119**, 161101 (2017).

[43] B. P. Abbott *et al.*, Multi-messenger observations of a binary neutron star merger, Astrophys. J. Lett. **848**, L12 (2017).

[44] B. P. Abbott *et al.*, GW170817: Measurements of Neutron Star Radii and Equation of State, Phys. Rev. Lett. **121**, 161101 (2018).

[45] M. C. Miller *et al.*, The radius of PSR J0740+6620 from NICER and XMM-Newton data, Astrophys. J. Lett. **918**, L28 (2021).

[46] T. E. Riley *et al.*, A NICER view of the massive pulsar PSR J0740+6620 informed by radio timing and XMM-Newton spectroscopy, Astrophys. J. Lett. **918**, L27 (2021).

[47] M. Bando, T. Kugo, and K. Yamawaki, Nonlinear realization and hidden local symmetries, Phys. Rep. **164**, 217 (1988).

[48] M. Harada and K. Yamawaki, Hidden local symmetry at loop: A new perspective of composite gauge boson and chiral phase transition, Phys. Rep. **381**, 1 (2003).
[49] G. Baym, S. Furusawa, T. Hatsuda, T. Kojo, and H. Togashi, New neutron star equation of state with quark-hadron crossover, Astrophys. J. **885**, 42 (2019).
[50] T. Hatsuda and T. Kunihiro, QCD phenomenology based on a chiral effective Lagrangian, Phys. Rep. **247**, 221 (1994).
[51] T. Kojo, P. D. Powell, Y. Song, and G. Baym, Phenomenological QCD equation of state for massive neutron stars, Phys. Rev. D **91**, 045003 (2015).
[52] R. C. Tolman, Static solutions of Einstein's field equations for spheres of fluid, Phys. Rev. **55**, 364 (1939).
[53] J. R. Oppenheimer and G. M. Volkoff, On massive neutron cores, Phys. Rev. **55**, 374 (1939).
[54] T. Kojo, QCD equations of state and speed of sound in neutron stars, AAPPS Bull. **31**, 11 (2021).
[55] G. Baym, C. Pethick, and P. Sutherland, The ground state of matter at high densities: Equation of state and stellar models, Astrophys. J. **170**, 299 (1971).
[56] A. Akmal, V. R. Pandharipande, and D. G. Ravenhall, The equation of state of nucleon matter and neutron star structure, Phys. Rev. C **58**, 1804 (1998).
[57] T. Kojo, Phenomenological neutron star equations of state: 3-window modeling of QCD matter, Eur. Phys. J. A **52**, 51 (2016).
[58] H. Togashi, K. Nakazato, Y. Takehara, S. Yamamuro, H. Suzuki, and M. Takano, Nuclear equation of state for core-collapse supernova simulations with realistic nuclear forces, Nucl. Phys. A **961**, 78 (2017).
[59] C. Drischler, S. Han, J. M. Lattimer, M. Prakash, S. Reddy, and T. Zhao, Limiting masses and radii of neutron stars and their implications, Phys. Rev. C **103**, 045808 (2021).
[60] T. Kojo, G. Baym, and T. Hatsuda, Implications of NICER for neutron starmatter: The QHC21 equation of state, ApJ **934**, 46 (2021).
[61] Y. Song, G. Baym, T. Hatsuda, and T. Kojo, Effective repulsion in dense quark matter from nonperturbative gluon exchange, Phys. Rev. D **100**, 034018 (2019).
[62] L. McLerran and S. Reddy, Quarkyonic Matter and Neutron Stars, Phys. Rev. Lett. **122**, 122701 (2019).
[63] T. Kojo, Stiffening of matter in quark-hadron continuity, Phys. Rev. D **104**, 074005 (2021).
[64] Y.-J. Huang, L. Baiotti, T. Kojo, K. Takami, H. Sotani, H. Togashi, T. Hatsuda, S. Nagataki, and Y.-Z. Fan, Merger and Post-Merger of Binaryneutron Stars With a Quark-Hadron Crossover Equation of State, Phys. Rev. Lett. **129**, 181101 (2022).
[65] T. Kojo and D. Suenaga, Peaks of sound velocity in two color dense QCD: Quark saturation effects and semishort range correlations, Phys. Rev. D **105**, 076001 (2022).
[66] K. Iida and E. Itou, Velocity of sound beyond the high-density relativistic limit from lattice simulation of dense two-color QCD (unpublished).
[67] B.-A. Li, B.-J. Cai, W.-J. Xie, and N.-B. Zhang, Progress in constraining nuclear symmetry energy using neutron star observables since GW170817, Universe **7**, 182 (2021).
[68] X. Wu, A. Ohnishi, and H. Shen, Effects of quark-matter symmetry energy on hadron-quark coexistence in neutron-star matter, Phys. Rev. C **98**, 065801 (2018).
[69] I. Tews, J. M. Lattimer, A. Ohnishi, and E. E. Kolomeitsev, Symmetry parameter constraints from a lower bound on neutron-matter energy, Astrophys. J. **848**, 105 (2017).
[70] C. Drischler, R. J. Furnstahl, J. A. Melendez, and D. R. Phillips, How Well Do We Know the Neutron-Matter Equation of State at the Densities Inside Neutron Stars?: A Bayesian Approach with Correlated Uncertainties, Phys. Rev. Lett. **125**, 202702 (2020).
[71] Y.-B. Yang, A. Alexandru, T. Draper, J. Liang, and K.-F. Liu, πN and strangeness sigma terms at the physical point with chiral fermions, Phys. Rev. D **94**, 054503 (2016).
[72] A. Abdel-Rehim, C. Alexandrou, M. Constantinou, K. Hadjiyiannakou, K. Jansen, Ch. Kallidonis, G. Koutsou, and A. Vaquero Aviles-Casco, Direct Evaluation of the Quark Content of Nucleons from Lattice QCD at the Physical Point, Phys. Rev. Lett. **116**, 252001 (2016).
[73] G. S. Bali, S. Collins, D. Richtmann, A. Schäfer, W. Söldner, and A. Sternbeck, Direct determinations of the nucleon and pion σ terms at nearly physical quark masses, Phys. Rev. D **93**, 094504 (2016).
[74] N. Yamanaka, S. Hashimoto, T. Kaneko, and H. Ohki, Nucleon charges with dynamical overlap fermions, Phys. Rev. D **98**, 054516 (2018).
[75] V. Kleinhaus, M. Buballa, D. Nickel, and M. Oertel, Pseudoscalar goldstone bosons in the color-flavor locked phase at moderate densities, Phys. Rev. D **76**, 074024 (2007).
[76] V. Kleinhaus and M. Buballa, Pseudoscalar bosonic excitations in the color-flavor locked phase at moderate densities, Phys. Rev. D **79**, 014016 (2009).
[77] T. Kojo, Pseudo Nambu–Goldstone modes in neutron stars, Phys. Lett. B **769**, 14 (2017).
[78] D. T. Son and M. A. Stephanov, Inverse meson mass ordering in color flavor locking phase of high density QCD, Phys. Rev. D **61**, 074012 (2000).
[79] M. Rho, A. Wirzba, and I. Zahed, Generalized pions in dense QCD, Phys. Lett. B **473**, 126 (2000).
[80] S. R. Beane, P. F. Bedaque, and M. J. Savage, Meson masses in high density QCD, Phys. Lett. B **483**, 131 (2000).
[81] P. F. Bedaque and T. Schäfer, High density quark matter under stress, Nucl. Phys. A **697**, 802 (2002).
[82] N. Yamamoto, M. Tachibana, T. Hatsuda, and G. Baym, Phase structure, collective modes, and the axial anomaly in dense QCD, Phys. Rev. D **76**, 074001 (2007).